Noninvasive Vascular Modulography Method for Imaging the Local Elasticity of Atherosclerotic Plaques: Simulation and *In Vitro* Vessel Phantom Study

Jonathan Porée, Boris Chayer, Gilles Soulez, Jacques Ohayon, and Guy Cloutier, *Senior Member, IEEE*

Abstract—Mechanical and morphological characterization of atherosclerotic lesions in carotid arteries remains an essential step for the evaluation of rupture prone plaques and the prevention of strokes. In this paper, we propose a noninvasive vascular imaging modulography (NIV-iMod) method, which is capable of reconstructing a heterogeneous Young's modulus distribution of a carotid plaque from the Von Mises strain elastogram. Elastograms were computed with noninvasive ultrasound images using the Lagrangian speckle model estimator and a dynamic segmentation-optimization procedure to highlight mechanical heterogeneities. This methodology, based on continuum mechanics, was validated *in silico* with finite-element model strain fields and ultrasound simulations, and *in vitro* with polyvinyl alcohol cryogel phantoms based on magnetic resonance imaging geometries of carotid plaques. *In silico*, our results show that the NiV-iMod method: 1) successfully detected and quantified necrotic core inclusions with high positive predictive value (PPV) and sensitivity value (SV) of $81\pm10\%$ and $91\pm6\%$; 2) quantified Young's moduli of necrotic cores, fibrous tissues, and calcium inclusions with mean values of 32 ± 23, 515 ± 30, and 3160 ± 218 kPa (ground true values are 10, 600, and 5000 kPa); and 3) overestimated the cap thickness by ~172 μm. *In vitro*, the PPV and SV for detecting soft inclusions were $60\pm21\%$ and $88\pm9\%$, and Young's modulus mean values of mimicking lipid, fibrosis, and calcium were 34 ± 19, 193 ± 14, and 649 ± 118 kPa (ground true values are 25 ± 3, 182 ± 21, and 757 ± 87 kPa).

Index Terms—Carotid plaques, inverse problem, noninvasive vascular elastography (NIVE), noninvasive vascular modulography.

I. INTRODUCTION

ISCHEMIC strokes and myocardial infractions, which are major causes of death worldwide [1]–[3], are mostly triggered by atherosclerotic plaque rupture [4]. Vulnerable plaques possess specific biological [5], morphological [6]–[8], and mechanical [9]–[14] features that need to be assessed to prevent rupture.

Noninvasive imaging tools such as magnetic resonance imaging (MRI) [15], computed tomography [16], [17], and ultrasound [18]–[20] have been developed to evaluate the morphology (i.e., degree of stenosis, necrotic core area, and plaque boundary), tissue content (e.g., fiber, lipid, and calcium), and biological processes (e.g., active inflammation) involved in atherosclerotic plaque progression. However, none of these methods can provide biomechanical features such as the plaque rigidity and peak cap stress (i.e., the maximum stress inside the fibrous cap), which are markers of plaque stability and vulnerability [11], [14], [21]–[23].

Inspired by the earliest work of Ophir *et al.* [24], invasive vascular elastography methods [25]–[27], and noninvasive vascular elastography (NIVE) [28]–[30] methods have successfully been developed to provide clinicians with quantitative measurements of the vessel deformation under physiological stress (i.e., blood pressure pulsation). Schmitt *et al.* [31] reported up to 20% of cumulated strain (in systole) for normal sections of carotids and 2% for atherosclerotic tissues containing calcium. Wan *et al.* [32] and Naim *et al.* [33] also reported up to 20% of cumulated strains with about $\sim1\%$ of instantaneous deformation (i.e., between two successive ultrasound images). According to Holzapfel *et al.* [34], with such ranges of deformation for instantaneous image frames (i.e., with typically $<1\%$ deformation), vascular tissues can be considered linear. Nonlinear behavior can be assessed when considering cumulated strains.

Hansen *et al.* [35] recently demonstrated that NIVE allows differentiation between fibrous and (fibro) atheromatous carotid plaques. A few groups also attempted to use dynamic elastography (i.e., acoustic radiation force impulse or supersonic shear imaging) to characterize vascular wall elasticity [36]–[38]. Such methods could not, however, provide a direct reading of the vessel wall internal morphology (i.e., necrotic core, calcium inclusions, and cap thickness), and elasticity of plaque components, because of the inability to detect intraplaque heterogeneities. To that end, Young's

modulus reconstruction methods of atherosclerotic plaques (i.e., modulograms) have been proposed.

By considering intravascular ultrasound (IVUS) scans of coronary arteries, Baldewsing *et al.* [39], [40] proposed to match parametric finite-element models (PFEMs) to the radial strain. In those studies, mechanical heterogeneities were identified by thresholding the strain distribution (i.e., high strains corresponding to soft tissues) and by matching parametric plaque geometries. Such methods, however, are dependent on the threshold level since it overlooked the internal stress decay (and thus strain decay) as a function of the radial distance that is characteristic of cylindrical geometry [41]. To overcome this problem, Le Floc'h *et al.* proposed a method based on continuum mechanics using an approximation of the gradient elasticity amplitude that is independent of the stress/strain decay [42]–[44].

In the context of NIVE of carotid arteries, alternative methods have been proposed to recover modulograms of the vascular wall. Hansen *et al.* [45] used angular compounding with the model-based elastography method described in [46] and [47] to recover modulograms from measured displacements on cross-sectional arteries. In their method, however, the shape and location of mechanical heterogeneities must be known *a priori*. In a recent study [48], they suggested to recover modulograms from axial strain measurements using NIVE. However, unlike intravascular methods, their approach requires the knowledge of the internal morphology of the plaque (i.e., the segmentation of necrotic cores and calcium inclusions) from *a priori* MRI measurements.

In this paper, to overcome this problem, we propose a fully automatic approach [noninvasive vascular imaging modulography (NIV-iMod)] to compute modulograms from NIVE measurements without *a priori* knowledge on the internal morphology of the plaque. The inverse problem is formulated as a segmentation/optimization procedure using continuum mechanics theory. Mechanical heterogeneities are dynamically segmented from the "apparent Young modulus (AYM) map," which is defined as the ratio of the Von Mises stress distribution, modeled using the finite-element (FE) method, and the measured Von Mises strain. The AYM criterion is iteratively updated to account for internal stress variations associated with the internal morphology of the plaque. Unlike previous methods, this approach only requires the measured Von Mises strain field, the internal and external contours of the vascular wall, and the loading condition (i.e., the systemic blood pressure).

The proposed method was validated, *in silico* on ten plaque morphologies, extracted from a previous MRI study [33] and modeled using the FE method. The robustness and performance of the proposed method were also evaluated on measured strain elastograms from simulated ultrasound images and *in vitro* on polyvinyl alcohol cryogel (PVA-c) vessel phantoms containing mimicking plaques.

II. MATERIALS AND METHODS

To study the performance of the proposed NIV-iMod algorithm, cross-sectional images of ten vulnerable plaques were selected from a series of patients who underwent high-resolution multicontrast MRI of the internal carotid artery [33]. Cross-sectional plaque morphologies (i.e., lumen, necrotic core, and calcium inclusions) were modeled using an FE model (FEM) software to simulate displacements and strain elastograms. These geometries were also used to simulate high-resolution ultrasound images. One of these geometries was used to build vessel mimicking phantoms for *in vitro* validation.

A. MRI Study and Plaque Geometries

1) MRI Acquisitions: Using a 1.5-T MRI unit (Siemens, Avanto, Erlangen, Germany) and a dedicated custom made four-element radio frequency (RF) surface coil developed in-house, cross-sectional images of carotid arteries were acquired and analyzed following the protocol of Naim *et al.* [33]. Each carotid artery was scanned from 1 cm below to 3 cm above the bifurcation. Ten cross-sectional images deemed vulnerable according to MRI criteria were selected (i.e., presence of a thin fibrous cap, or of a large necrotic core area $> 25\%$ of the total plaque area, or presence of neovascularization). Details on MRI plaque vulnerability analysis can be found in [49].

2) MRI Image Analysis: For each selected image, vessel contours and tissue components (necrotic core, calcifications, and fibrous tissue) were manually traced using a segmentation software program (QPlaque MR 1.0.16, Medis, The Netherlands).

3) MRI Measurements and Definitions: Each cross-sectional MRI image was quantitatively analyzed. Measurements were made for the wall area ($Wall_{area}$, mm^2); lumen area (Lu_{area}, mm^2); necrotic core area (Nc_{area}, mm^2); calcium area ($Calc_{area}$, mm^2); degree of stenosis ($Stenos_{deg}$, %), defined as $100 \times Wall_{area}/(Wall_{area} + Lu_{area})$; and cap thickness ($Cap_{thick}$, mm), defined as the shortest distance between the lumen and the necrotic core.

B. Forward Problem: Spatial Strain Distribution From Structural Analysis Using Finite-Element Modeling and In Vitro Experiments

Static FE computations were performed on all geometries and three *in vitro* phantom experiments were conducted based on the geometry of Plaque #1. For FE simulations, the spatial displacement and strain distributions were calculated using COMSOL multiphysics software (Structural Mechanics Module, version 3.3, COMSOL, France), whereas they were experimentally measured for phantom (i.e., *in silico* and *in vitro*) validations. Fig. 1 summarizes the successive steps involved in the forward problem.

1) Boundary Conditions, Material Properties, and Loading of FE Simulations: The digitized contours extracted from Qplaque were imported into MATLAB (The MathWorks, Natick, MA, USA) and then transferred into COMSOL to build FE models. These models were solved under the assumption of plane strain and a blood pressure differential of 0.5 kPa (or 4 mmHg between considered consecutive ultrasound images) was applied. To simulate free boundary conditions on the external contour, a very soft (1 Pa) and compressible
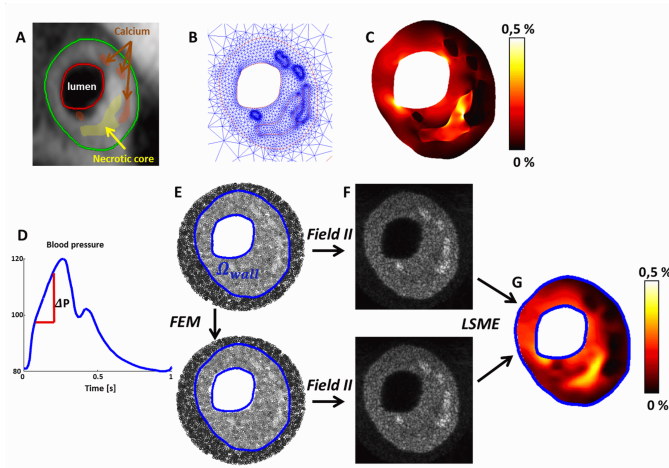
Fig. 1. Flowchart describing the forward problem. (a) Typical T1-weighted MRI of an internal carotid artery segmented with QPlaque. (b) FEM of the plaque. (c) Ground truth Von Mises strain field extracted from the FEM. (d) Blood pressure curve used for the loading. (e) Acoustic model of the plaque (before and after loading). (f) Simulated ultrasound B-mode images (before and after loading). (g) Von Mises strain field measured from ultrasound images using the LSME algorithm.

(Poisson's ratio $\nu = 0.001$) layer of 1-mm thickness was added on the outer layer. The outer contour of this artificial layer was anchored to prevent rigid body motion during FEM computation and was not considered in the strain analysis. The fibrosis, calcium, and soft necrotic core were modeled as isotropic quasi-incompressible solids ($\nu = 0.49$) with Young's moduli $E_{fib} = 600$ kPa, $E_{calc} = 5000$ kPa, and $E_{nc} = 10$ kPa, respectively, as in [12], [42], and [50]. The entire plaque geometries were meshed with approximately $15\,000$ six-node triangular elements. To simulate realistic pulsating conditions, one geometry (Plaque #1) was also loaded with a systemic blood pressure waveform (one cardiac cycle) with minima and maxima at 80 and 120 mmHg (10 and 16 kPa), respectively (see Fig. 1). This waveform was discretized to simulate an ultrafast noninvasive ultrasound acquisition at a frame rate of 500 s^{-1} [30]. The time step was varied afterward to evaluate the impact of the loading conditions on the modulus reconstruction performance (see Fig. 6).

2) Ultrasound Simulation Based on the Displacement Field: Acoustic models of plaque geometries were created by randomly distributing point scatterers over the cross section of the vessel wall. To ensure a fully developed speckle, the scatterer density was chosen at 100 per resolution cell [51]. The displacement field generated by COMSOL was considered to move scatterers to create the postdeformation acoustic model of the artery. The Field II simulation program [52] was used to mimic the 128 elements of the L14-5/38 linear array probe (Ultrasonix, Analogic Ultrasound, Vancouver, Canada) characterized by a 7.2-MHz center frequency sampled at 40 MHz. High-resolution compound plane wave (CPW) images were simulated using 64 tilted plane wave emissions (from $-15°$ to $15°$) and a time overlap of 30% to mimic an effective frame rate of 500 s^{-1}. The delay and sum algorithm [53] was used to reconstruct high-resolution RF images on a regular Cartesian grid with half wavelength resolution ($\sim$100 μm $\times$ 100 μm). An image depth of 30 mm

was considered and the carotid vessel was positioned at 15-mm depth. White Gaussian noise was added on RF channel data prior to beamforming to simulate electronic noise induced by the acquisition system.

3) In Vitro Polyvinyl Alcohol Cryogel Vessel Phantom Study: The mimicking arteries were fabricated with the PVA-c tissue mimicking material. The stiffness of PVA-c increases with the number of freeze-thaw cycles used for its polymerization. The preparation protocol followed the methodology described in [54]. The solution had a concentration of 10% by weight of polyvinyl alcohol dissolved in pure water and ethanol homopolymer. The weight percentage of added particles used as acoustic scatterers (Sigmacell cellulose, type 50, Sigma Chemical, St. Louis, MO, USA) was 3%. One to three freezing-thawing cycles were considered, using a specifically designed temperature-controlled chamber [54]. A mold was first designed using a 3-D printer (Dimension Elite 3-D printer, Stratasys, Eden Prairie, MN, USA) and three vessel phantoms were generated. The first phantom was homogeneous without any inclusion (3 freeze-thaw cycles giving an elasticity $E = 182 \pm 21$ kPa, as measured by tensile test [54]). The second phantom had a soft inclusion modeling the necrotic core geometry of Plaque #1 (1 freeze-thaw cycle with $E = 25 \pm 3$ kPa [54]). The remaining of the artery had the same mean elasticity as the first phantom. For the third phantom, we considered the same geometry as Plaque #1 but in addition to the soft plaque inclusion, we added polyurethane hard inclusions. The rigidity of polyurethane was measured at $E = 757 \pm 87$ kPa with a uniaxial rheometer (Bose Enduratec ELF 3200, Eden Prairie, MI, USA).

4) Strain Estimation: For both ultrasound simulations and *in vitro* experiments performed with the Ultrasonix scanner using the same settings as in the simulations, we used the Lagrangian speckle model estimator (LSME), with the assumption of plane strain deformation and tissue incompressibility [30] to compute the 2-D deformation matrix ($\Delta_{xx}, \Delta_{xz}, \Delta_{zz}, \Delta_{zx}$) in the (x, z) imaging plane (x stands for the lateral direction and z for the axial/in-depth direction). The first step of this method consisted in a local rigid registration on overlapping measurement windows (MWs) to compensate for potential translation movement using 2-D ensemble correlation. This step was followed by a least-square estimation of the optical flow solution using a 2-D deformation model for each MW. A robust smoothing of the displacement and strain fields followed each steps (for noise cancelation and outliers rejection). The size of each MW was 1 mm $\times$ 1 mm in space and a time-ensemble estimation over eight successive frames (16 ms) was considered, as in [30]. The spatial and time overlaps of MWs were set to 90% to get high-sampled elastograms. The Von Mises strain coefficient ε was computed using the following expression:

$$\varepsilon_{VM} = \sqrt{\Delta_{xx}^2 + \Delta_{zz}^2 - \Delta_{xx}\Delta_{zz} + \frac{3}{4}(\Delta_{xz} + \Delta_{zx})}. \quad (1)$$

C. Inverse Problem: Elasticity Reconstruction Method

The vessel wall domain Ω_{wall} (see Fig. 1) was assumed to be isotropic, heterogeneous, and quasi-incompressible

(Poisson's ratio $v = 0.49$), and was described by the linear elastic Hooke's law

$$[\sigma(\vec{x})] = \frac{E(\vec{x})}{1+v}\left(\frac{v}{1-2v}\text{Trace}[\varepsilon(\vec{x})][I] + [\varepsilon(\vec{x})]\right) \quad (2)$$

where $[\sigma(\vec{x})]$ and $[\varepsilon(\vec{x})]$ are the stress and strain tensors, respectively, $[I]$ is the identity matrix, and E the Young's modulus, which is an arbitrary function of the position $\vec{x} = (x, z)$. Assuming the incompressibility of the constitutive elements of the vascular wall, the strain tensor $[\varepsilon]$ satisfies the following equation:

$$\text{Trace}[\varepsilon(\vec{x})] = 0. \quad (3)$$

Substituting (3) into (2) allowed obtaining the following simplified relation:

$$[\sigma(\vec{x})] = \frac{E(\vec{x})}{1+v}[\varepsilon(\vec{x})]. \quad (4)$$

By extension, the Von Mises stress σ_{VM} is related to the Von Mises strain ε_{VM} by the same relation.

1) Enhancement of Mechanical Heterogeneities Based on Continuum Mechanics: Assuming plane strain condition, the mathematical problem becomes well defined because boundary conditions, at the inner ($\partial\Omega_{wall}^{in}$) and outer ($\partial\Omega_{wall}^{out}$) vessel walls, are given in terms of the imposed stresses. At the outer limit ($\partial\Omega_{wall}^{out}$), a zero pressure can be assumed while at the inner limit ($\partial\Omega_{wall}^{in}$), a blood pressure gradient $\Delta P = 0.5$ kPa was applied, as in [42]

$$[\sigma(\vec{x})] \cdot \vec{n} = -\Delta P\vec{n} \quad \text{on } \partial\,\Omega_{wall}^{in} \quad (5)$$

where $\vec{n}$ is the external unit vector normal to the contour $\partial\Omega_{wall}^{in}$.

Knowing boundary conditions and assuming at the initial step ($k = 0$) that the vessel wall behaves as a mechanically homogeneous tissue with a Young's modulus $E_{init} = 600$ kPa, the homogeneous stress tensor field $[\sigma^0]$ can be computed using a PFEM implemented in COMSOL. From this initial stress field, the AYM^1 can be defined as

$$AYM^k(\vec{x}) = (1+v)\frac{\sigma_{VM,PFEM}^{k-1}(\vec{x})}{\varepsilon_{VM,meas}(\vec{x})} \quad (6)$$

where $\sigma_{VM,PFEM} = (\sigma_{xx}^2 + \sigma_{zz}^2 - \sigma_{xx}\sigma_{zz} + 3\sigma_{xz}^2)^{1/2}$ is the Von Mises stress coefficient computed with the PFEM. The parameter AYM (see Fig. 2) highlights heterogeneities in elasticity of the vessel wall components and is further used as a segmentation criterion. Note that if the real stress is used in (6) then we have $AYM = E(\vec{x})$.

2) Segmentation of Mechanical Heterogeneities: This step was performed using a K-means clustering algorithm [55] applied on AYM_{log}^k (logarithmic scale). Three clusters were initialized using the expected Young's moduli of tissue components (necrotic core, fibrotic tissue, and calcium with $E_{nc} = 10$ kPa, $E_{fib} = 600$ kPa, and $E_{calc} = 5000$ kPa, respectively). The K-means algorithm provided three (or less) regions (clusters) with relatively homogeneous elasticity (Ω_{nc}, Ω_{fib}, and Ω_{calc}), from which the contours of the elasticity heterogeneities (see black contours overlaid on the AYM criterion
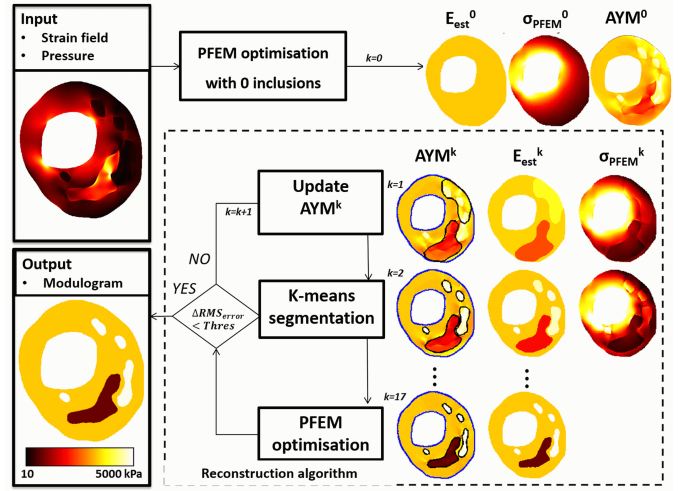

Fig. 2. Flowchart describing the inverse problem. The PFEM is initialized with the inner and outer contours of the vessel wall and assumed mechanically homogeneous ($E_0 = 600$ kPa). The PFEM is solved using an inner pressure $\Delta P = 0.5$ kPa to give the homogeneous Von Mises stress field σ_{PFEM}. Equation (6) gives the AYM, which is used as a segmentation criterion of plaque inclusions. The problem is then iteratively solved updating the Von Mises stress field σ_{PFEM}^k and AYM^K until convergence. A detailed description is given in Section II-C.

in Fig. 2) were derived and used in the PFEM as preconditioning regions. More clusters could be initialized to provide a more detailed segmentation of the plaque but at the expense of computational complexity. In this paper, we only considered three clusters as the MRI models provided three sets of tissue components.

3) Young's Modulus Estimation: At each iteration k of the reconstruction algorithm, the AYM issued from the previous iteration (AYM_{log}^{k-1}) was segmented using the K-means clustering algorithm. This procedure provided a partition of the vessel wall domain Ω_{wall} into n unconnected inclusions ($\Omega_{1...n}$) whose respective stiffness's were assumed uniform. The n Young's moduli were then identified using a gradient-based optimization procedure (fmincon, Optimization Toolbox, MATLAB, release R14, The MathWorks), which minimized the root mean squared error ($RMS_{wall-error}$) between the FE modeled von Mises strain field $\varepsilon_{VM,PFEM}^k$ and the measured Von Mises strain field $\varepsilon_{VM,meas}$, as given by:

$$RMS_{wall-error}^k = \sqrt{\frac{1}{N}\sum_{n_i}\left[\varepsilon_{VM,meas}(n_i) - \varepsilon_{VM,PFEM}^k(n_i)\right]^2} \quad (7)$$

where N is the total number of nodes in the wall mesh, and n_i is the node i of the mesh.

One constraint was imposed during the optimization procedure: unknown Young's moduli were limited between 1 and 10 000 kPa. A set of Young's modulus solution was found acceptable when the gradient-based optimization reached either a tolerance termination on the maximum strain $\Delta RMS_{wall-error}^{k,l} = (RMS_{wall-error}^{k,l} - RMS_{wall-error}^{k,l-1}) < 5\%$ (l being the iteration of the optimization procedure) or a maximum number of iterations of $l = 20$. To prevent the optimization to fall into local minima, Young's moduli E_n

TABLE I

DESCRIPTION OF PLAQUE CHARACTERISTICS BASED ON MRI

Plaque #	Cap_{thick} (mm)	$Core_{area}$ (mm²)	$Calc_{area}$ (mm²)	$Wall_{area}$ (mm²)	Lu_{area} (mm²)	$Sten_{deg}$ (%)
1	1.5	11.3	7.4	111.8	26.9	80.6
2	1.5	20.7	7.7	115.8	27.7	80.7
3	1.6	15.8	-	55.2	3.1	94.6
4	1.2	9.7	-	46.9	5.9	88.8
5	2.3	7.5	-	55.7	4.8	92.1
6	1.8	46.9	-	133.7	3.6	97.6
7	2.5	48.9	2.1	134.4	3.6	97.4
8	0.2	3.0	-	34.3	8.2	80.8
9	1.4	4.8	-	31.9	10.5	75.3
10	0.1	4.5	-	23.7	11.0	68.4

of all inclusions delimited by Ω_n were initialized, close to the expected solutions, using the following expression:

$$E_n^{\text{init}} = \frac{1}{N_n} \sum_{n_i \in \Omega_n} \text{AYM}^{k-1}(n_i) \qquad (8)$$

which gave the average of the AYM criterion, over the region Ω_n (N_n being the number of nodes inside the region Ω_n).

4) Overall Segmentation/Optimization Procedure: After optimization, the AYM map was updated (6) using the computed PFEM von Mises stress field, and used in the next iteration $(k+1)$ of the segmentation to update the internal morphologies of the plaque and the mesh of the PFEM. The overall segmentation/optimization procedure was stopped when the RMS$_{\text{wall-error}}$ variation between two successive iterations k and $k+1$ became negative (RMS$_{\text{wall-error}}^{k-1}$ < RMS$_{\text{wall-error}}^{k}$) or when the number of iterations k reached 100. In practice, the algorithm converged in about 20 iterations. Fig. 2 schematizes successive steps involved in the proposed iterative inverse problem approach to identify the elasticity map from the Von Mises strain field.

III. RESULTS

A. MRI Study

Ten plaques with necrotic cores and calcium inclusions were identified after MRI image analysis. Table I summarizes their geometrical features (Cap$_{\text{thick}}$, Core$_{\text{area}}$, Calc$_{\text{area}}$, Wall$_{\text{area}}$, Lu$_{\text{area}}$, Sten$_{\text{deg}}$) used for the validation of the proposed modulography algorithm.

B. FEM Study

Fig. 3 illustrates the performance of the proposed NIV-iMod algorithm to recover complex plaque morphologies, with necrotic cores (Plaques 3 and 8) and calcium inclusions (Plaques 1 and 2), and to estimate the Young's modulus of their components from the FEM strain field. Table II summarizes the performance of the proposed method on all geometries.

1) Validation of the Optimization Procedure: To validate the quantification of Young's moduli without the bias that estimated contours might introduce, we ran the optimization part of the algorithm using reference contours, extracted from MRI, as preconditioning regions. The results are presented in Table II in columns NIV-iMod Manual. Overall, using real
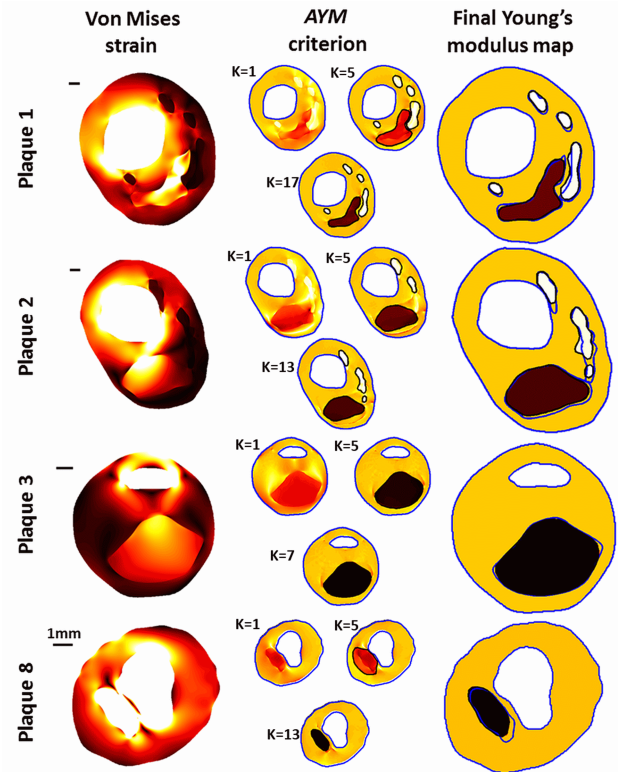

Fig. 3. Performance of the method to obtain morphologies and modulograms from FE strain fields. Four strain fields issued from FE models of carotid plaques (Plaques #1, 2, 3, and 8) were used for this investigation. Column 1: Von Mises strain field obtained with a blood pressure of 0.5 kPa. Column 2: evolution of the AYM map and segmentation during the execution of the iterative segmentation/optimization approach. Column 3: final Young's modulus map and segmentation of internal components of the plaque. Iterative and final segmentation contours are displayed in black, while reference contours are in blue. Quantitative results on the effectiveness of the segmentation and estimation of Young's moduli are given in Table II.

FEM strain fields as input, Young's moduli were consistent with values of 14 ± 4 kPa for necrotic cores (true value of 10 kPa), 4840 ± 70 kPa for calcium inclusions (5000 kPa), and 600 ± 6 kPa for fibrosis (600 kPa).

2) Validation of the Segmentation Procedure: To test the performance of the segmentation algorithm, we compared computed contours of inclusions to real ones (extracted from the MRI analysis), using the following indexes: 1) the positive predictive value (PPV), defined as the ratio between the "true positive area" and the union of the "true positive area" with the "false positive area" and 2) the sensitivity value (SV), defined as the ratio between the "true positive area" and the union of the "true positive area" with the "false negative area." Overall, whatever the geometry (Plaques #1–10), PPV and SV indexes for the necrotic cores were greater than 73.5% and 77.6% with an average of $94.4 \pm 7.3\%$ and $87.6 \pm 5.1\%$, respectively. For calcium inclusions, PPV and SV were greater than 15.5% and 80.3% with an average of $61.8 \pm 32.8\%$ and $88.5 \pm 7.4\%$.

3) Quantification of the Cap Thickness: The cap thickness error (Cap$_{\text{thick}}$ error in μm) was defined as the signed difference between real and computed ones (a negative error means an underestimation of the cap thickness). The maximum

TABLE II

ANALYSIS OF THE PERFORMANCE OF NIV-IMOD. COMPARISON BETWEEN COMPUTED AND MRI PLAQUE MORPHOLOGY INDICES AND YOUNG'S MODULI ARE PRESENTED. THE ACCURACY OF THE APPROACH WAS INVESTIGATED BY USING THE FEM (FEM STUDY), ULTRASOUND SIMULATED (FIELD II STUDY), AND REAL (*In Vitro* STUDY) ULTRASOUND IMAGES. PPV: PREDICTIVE POSITIVE VALUE. SV: SENSITIVITY VALUE. NIV-IMOD MANUAL: OPTIMIZATION APPROACH WITH KNOWN MRI CONTOURS. NIV-IMOD AUTO: PROPOSED SEGMENTATION/OPTIMIZATION ITERATIVE APPROACH

Plaque #	*Plaque morphology*					*Intra-plaque Young's moduli*					
	Necrotic core		Cap_{thick}	Calcium		Necrotic core NIV-iMod Auto/Manual		Fibrosis NIV-iMod Auto/Manual		Calcium NIV-iMod Auto/Manual	
	PPV(%)	SV(%)	Error (μm)	PPV(%)	SV(%)						
FEM study						**(10 kPa)**		**(600 kPa)**		**(5000 kPa)**	
1	96.2	93.4	-118	85.2	87.0	25	22	604	597	4633	4857
2	98.7	90.6	-42	84.8	80.3	19	16	614	602	4185	4747
3	99.8	97.4	81			10	11	593	602		
4	97.2	86.9	-17			10	14	598	604		
5	97.8	87.8	47			13	18	607	613		
6	94.8	87.6	228			5	12	591	593		
7	98.5	85.2	-49	15.5	98.3	16	10	582	596	2149	4917
8	91.3	86.3	37			8	11	579	600		
9	95.9	77.6	36			15	15	585	602		
10	73.5	83.4	115			28	12	519	592		
mean	94.4	87.6	77	61.8	88.5	15	14	587	600	3655	4840
±std	±7.3	±5.1	±60	±32.8	±7.4	±7	±4	±25	±6	±1081	±70
Field II study						**(10 kPa)**		**(600 kPa)**		**(5000 kPa)**	
1	83.5	94.3	-222	67.1	90.2	27	19	557	557	3269	3374
2	85.2	95.7	-229	56.7	89.5	28	18	518	530	3356	3854
3	93.1	97.2	53			8	14	489	478		
4	86.5	92.1	-158			9	12	532	495		
5	75.8	94.1	-391			72	54	529	500		
6	63.6	89.5	214			14	39	458	303		
7	91.5	73.8	-168	12.9	80.7	73	26	552	508	2856	2511
8	82.8	90.6	-141			48	32	522	522		
9	88.2	87.6	125			9	34	524	525		
10	63.2	90.1	-22			33	30	474	398		
mean	81.4	90.5	172	45.5	86.8	32	28	516	481	3160	3247
±std	±10.1	±6.2	±98	±23.5	±4.3	±23	±12	±30	±72	±218	±556
In vitro study						**(25 ± 3 kPa)**		**(182 ± 21 kPa)**		**(757 ± 87 kPa)**	
1	-	-	-	-	-	-	-	205±9	202±9	-	-
2	63±21	84±5	196±37	-	-	36±27	34±27	183±18	175±18		
3	56±24	92±11	168±257	57±3	51±3	33±14	24±5	192±7	186±5	649±118	568±206

absolute error for all plaques was of 228 μm (Plaque #6) with an absolute average of 77 ± 60 μm.

4) Accuracy of Computed Modulograms (With Estimated Contours): While Young's moduli of fibrosis and necrotic cores were reasonably identified with the proposed algorithm NIV-iMod Auto (means of 587 ± 25 and 15 ± 7 kPa, respectively, Table II), the stiffness of calcium inclusions were underestimated (means of 3655 ± 1081 kPa, Table II). The Young's modulus of the calcium inclusion of Plaque #7 was particularly difficult to estimate due to its small size (2149 ± 997 kPa versus 4917 kPa with the reference contour). On the other hand, using ground true FEM contours, the algorithm NIV-iMod performed well with estimated Young's moduli at 4840 ± 70 kPa for calcium inclusions.

C. Ultrasound Simulation Study

Fig. 4 illustrates the performance of the algorithm on measured strain fields computed with the LSME using ultrasound simulations.

1) Impact of Measured Strain Fields on Estimated Young's Moduli (With Real Contours): Using measured strain fields from ultrasound Field II simulations and real inclusion contours, estimated Young's moduli of soft inclusions were slightly overestimated at 28 ± 12 kPa (true value = 10 kPa), while calcium inclusions were significantly underestimated at 3247 ± 556 kPa (5000 kPa). Fibrosis was also slightly underestimated (481 ± 72 kPa versus 600 kPa).

2) Accuracy of Computed Modulograms (With Estimated Contours): While Young's moduli of fibrosis were reasonably identified (516 ± 30 kPa versus 600 kPa), the stiffness of calcium inclusions was again significantly underestimated (3160 ± 218 kPa), whereas that of soft inclusions was also overestimated (32 ± 23 kPa).

3) Performance of the Segmentation Procedure: Using measured strain fields as input for NIV-iMod Auto, soft inclusions were well detected (PPV = $81.4 \pm 10.1\%$ and SV = $90.5 \pm 6.2\%$ with minima at 63.2% and 76.8%, respectively). Hard inclusions were more difficult to detect (PPV = $45.5 \pm 23.5\%$ and SV = $86.8 \pm 4.3\%$ with minima at 12.9% and 80.7%, respectively). Regarding the cap thickness, the maximum absolute error was 390 μm (Plaque #5) and average values for all plaques were 172 ± 98 μm, which is close to the wavelength of the simulated ultrasound probe (L14-5/38, $\lambda \approx 200$ μm).

4) Influence of Ultrasound RF Noise and Loading Pressure ΔP on Computed Modulograms: Fig. 5 illustrates the influence of added white Gaussian noise on estimated Von Mises strain fields (first row), AYM map (second row), and computed
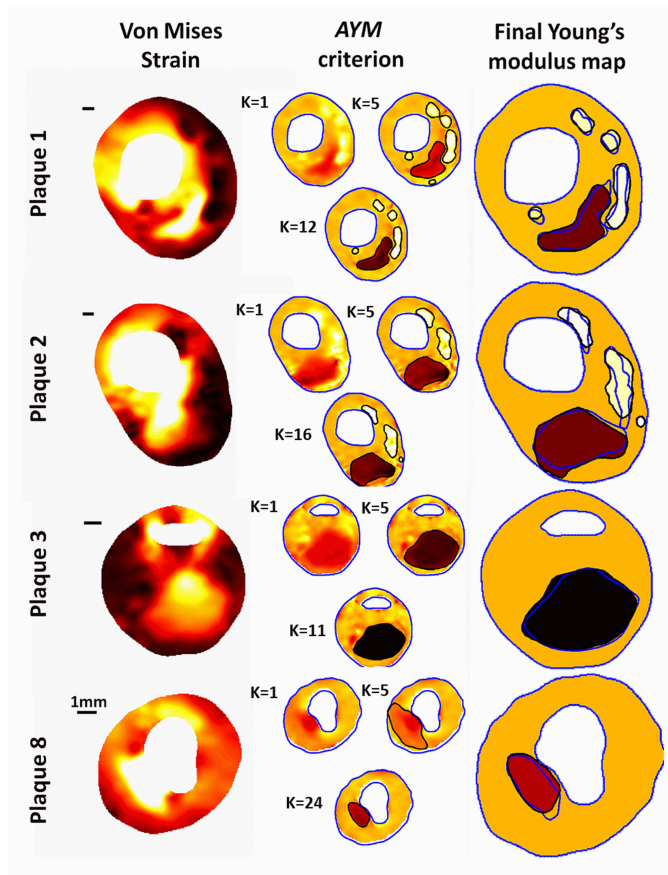
Fig. 4. Performance of the method to obtain morphologies and modulograms from ultrasound measured Von Mises strain fields. Four strain fields issued from FE models of carotid plaques (Plaques #1, 2, 3, and 8) were used for this investigation. Column 1: Von Mises strain field measured from ultrasound simulated images obtained with a blood pressure of 0.5 kPa. Column 2: evolution of the AYM map and segmentation during the execution of the iterative segmentation/optimization approach. Column 3: final Young's modulus map and segmentation of the internal morphologies. Iterative and final segmentation contours are displayed in black, while reference contours are displayed in blue. Quantitative results on the effectiveness of the segmentation and Young's modulus estimation are given in Table II.
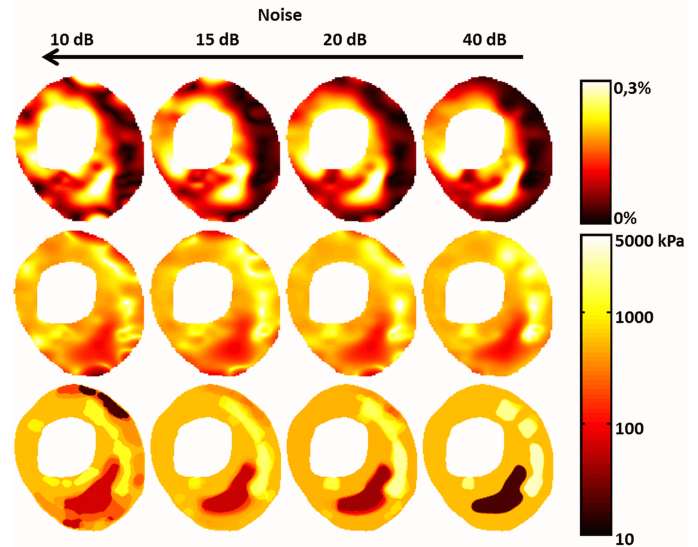

Fig. 5. Sensitivity analysis performed to investigate the influence of ultrasound noise. Plaque #1 with one necrotic core and four calcium inclusions was used for this investigation. Randomly distributed white Gaussian noise was added on simulated RF ultrasound data to reach a signal-to-noise ratio (SNR) from 40 to 10 dB. Row 1: Von Mises strain field measured using the LSME for a blood pressure gradient of 0.5 kPa. Row 2: AYM map at the first iteration of the NIV-iMod algorithm. Row 3: final Young's modulus map averaged over ten realizations of random noise addition.
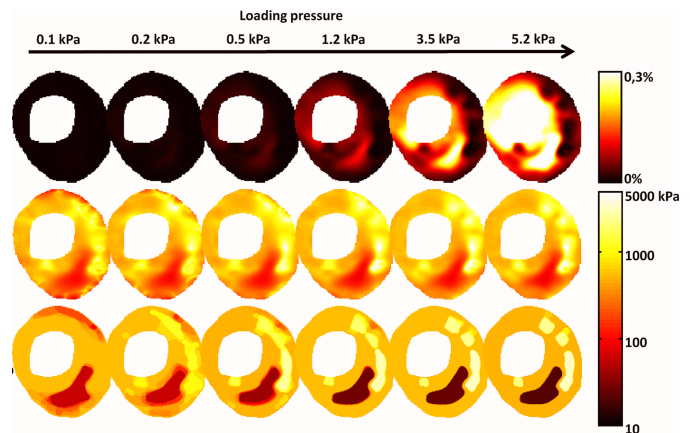
Fig. 6. Sensitivity analysis performed to investigate the influence of the loading pressure ΔP. Plaque #1 with one necrotic core and four calcium inclusions was used for this investigation. Randomly distributed white Gaussian noise was added on RF ultrasound data to reach an SNR of 20 dB. Row 1: Von Mises strain field measured using the LSME for a blood pressure gradient from 0.1 to 5.2 kPa. Row 2: AYM map at the first iteration of the NIV-iMod algorithm. Row 3: final Young's modulus map averaged over ten realizations of random noise addition.

modulograms (last row, average over ten independent realizations of noise addition) for an applied pressure $\Delta P = 0.5$ kPa between consecutive ultrasound images. As the noise level increases from 40 to 10 dB, the measured Von Mises strain field and computed AYM criterion present more and more artifacts, especially in high stiffness (or low deformation) regions. As a result, computed modulograms have artefactual inclusions with random stiffness values (low or high). The estimated stiffness of the soft inclusion increases and hard inclusions become more difficult to detect.

Fig. 6 illustrates the impact of the loading pressure on strain maps, AYM, and computed modulograms for a noise level of 20 dB. As the pressure gradient increases from 0.1 to 5.2 kPa (0.75–40 mmHg), the Von Mises strain becomes more contrasted. As a result, the AYM criterion is less noisy, especially for high stiffness (or low deformation) regions, and modulograms become more accurate. Fig. 7 shows the impact of the loading pressure on estimated modulograms. As the pressure gradient decreases, the inclusion detection

becomes inaccurate (see PPV and SV). At very low pressure, the contrast becomes insufficient to detect hard inclusions. Furthermore, the bias on estimated Young's moduli increases. At 0.2 kPa, detected necrotic core Young's moduli are overestimated (61 ± 25 kPa) and calcium inclusions are underestimated (1911 ± 582 kPa). At 0.1 kPa, calcium inclusions could not be detected. The pressure loading less influenced the detection of the cap thickness but more variances are detected at the lowest pressures.
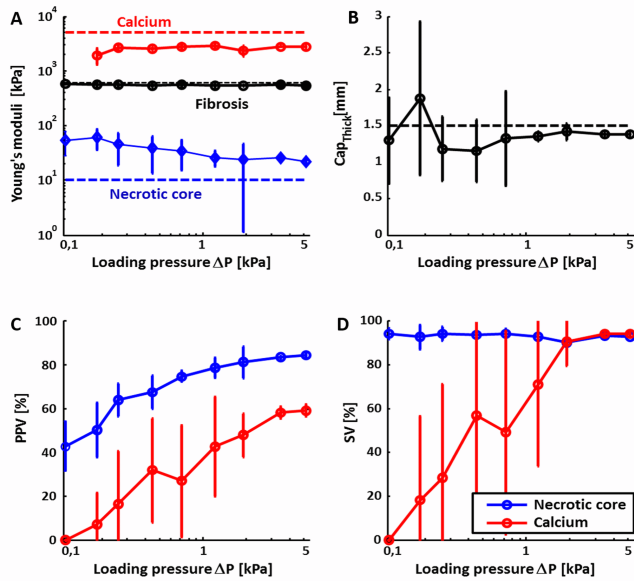
Fig. 7. Influence of the loading pressure ΔP on the performance of the algorithm. (a) Young's moduli of necrotic cores (blue line), fibrotic tissues (black line), and calcium inclusions (red line). (b) Cap thicknesses. (c) PPVs of necrotic cores (blue line) and calcium inclusions (red line). (d) SVs of necrotic cores (blue line) and calcium inclusions (red line). Plaque #1 was used for this investigation. For each pressure loading, ten computations were performed with randomly distributed noise at 20 dB.
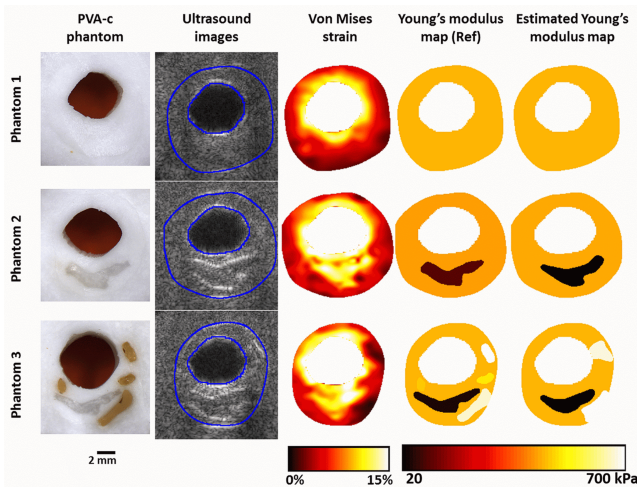

Fig. 8. Performance of the NIV-iMod method to detect soft and hard inclusions using the experimental ultrasound images acquired on three PVA-c phantoms modeled from Plaque #1. Column 1: cross sections of the three PVA-c phantoms. Column 2: ultrasound B-mode images obtained using CPW imaging. Column 3: cumulated Von Mises strain (over ~22 frames, $\Delta P \sim 0.5$ kPa) for a total loading pressure $\Delta P = 11$ kPa (80 mmHg). Column 4: AYM map at the first initialization ($k = 1$) of the NIV-iMod algorithm. Column 5: Young modulus map computed using the optimization part of the proposed method and manually segmented contour inclusions. Column 6: Young modulus map computed using the NIV-iMod algorithm.

D. Modulogram Reconstruction of PVA-c Phantoms

Fig. 8 illustrates the performance of the proposed NIV-iMod algorithm to detect the morphology of the three PVA-c vessel phantoms mimicking: a healthy vessel (Phantom #1) and two vulnerable plaques, one with a single soft inclusion (Phantom #2) and another with a soft inclusion and four hard inclusions (Phantom #3). Von Mises strain elastograms, AYM and Young's modulus maps from manually segmented and computed contours are presented. To evaluate reproducibility, three slices along the vessel were acquired independently. Quantitative results are presented in Table II.

1) Validation of the Automatic Segmentation: The accuracy of the segmentation was investigated using the cap thickness error, PPV, and SV metrics using the manual segmentation (from the photograph in Fig. 8) as reference for vessel Phantoms #2 and #3. For the second phantom, the soft inclusion was reasonably detected with PPV = $63 \pm 21\%$, SV = $84 \pm 5\%$, and a cap thickness error of 196 ± 37 μm (Cap$_{thick}$ = 1.5 mm). For the third phantom, the soft inclusion was also reasonably detected (PPV = $56 \pm 24\%$ and SV = $92 \pm 11\%$). Hard inclusions, however, were more difficult to detect with PPV = $57 \pm 3\%$ and SV = $51 \pm 3\%$. On average (over the 3 acquisitions), only 2 out of the four hard inclusions were detected. The error on the cap thickness was on the order of the wavelength (Cap$_{thick}$ = 168 ± 257 μm for a wavelength $\lambda \approx 200$ μm).

2) Performance of the Algorithm to Characterize a Healthy Vessel: The elasticity reconstruction performed on the homogeneous Phantom #1 is presented in the top row of Fig. 8. As expected, the NIV-iMod found neither soft nor hard inclusions, and estimated averaged Young's moduli within the segmented area at 205 ± 9 kPa (expected value $E = 182$ kPa). Using reference contours to constrain the algorithm, Young's moduli were estimated at 202 ± 9 kPa.

3) Performance of the Algorithm to Characterize a Plaque With a Complex Morphology: For both vulnerable vessel models (Phantoms #2 and #3, Fig. 8), Young's moduli of the mimicking fibrotic tissue were accurately estimated: 183 ± 18 and 192 ± 7 kPa, respectively (expected value = 182 ± 21 kPa). Soft inclusions were slightly overestimated and presented larger variability: 36 ± 27 and 33 ± 14 kPa (expected value = 25 ± 3 kPa). Hard inclusions and their Young's moduli were more difficult to detect. When detected, Young's moduli were underestimated at 649 ± 118 kPa (expected value = 757 ± 87 kPa).

IV. DISCUSSION

Quantifying biomechanical properties and internal morphologies of an atherosclerotic vascular wall could be of great interest for monitoring its remodeling and for the prevention of stroke [4], [5]. Arterial strain can be measured with relatively good accuracy using either endovascular elastography (EVE) or NIVE. However, the determination of plaque components (i.e., necrotic core, calcium inclusions, and fibrotic tissues), internal morphology (degree of stenosis, fibrous cap thickness, and necrotic core area), and their mechanical properties (Young's moduli) remain challenging because of the unknown stress distribution. A few studies [40], [44], based on EVE have successfully addressed this problem of solving the mechanical inverse problem, but *in vivo* reports have yet to come. Using NIVE, few methods have also been proposed to recover the Young modulus distribution of carotid plaques [45], [48]. However, those methods require the manual segmentation of tissue components from an adjacent modality (i.e., MRI), which remain a limitation for clinical application.

In this paper, we provided a robust solution for the reconstruction of the internal plaque morphology and Young's modulus based on NIVE. The modulography approach (NIV-iMod) combines a PFEM driven by a dynamic K-means segmentation method, for the detection of mechanical heterogeneities and the estimation of their Young's moduli. The NIV-iMod algorithm was successfully evaluated on FEM strain fields and strain elastograms computed from simulated and *in vitro* ultrasound images.

A. Performance of the Algorithm on FE Strain Fields

Using realistic models of rupture prone plaques, it was shown that the proposed inverse problem was very efficient in predicting the intraplaque Young's moduli from the Von Mises strain distributions and known contours (see NIV-iMod Manual in Table II), which confirms the stability of the proposed FE model. The dynamic segmentation approach based on the AYM criterion was found very efficient to detect mechanical heterogeneities (see NIV-iMod Auto in Table II). Unlike EVE-based modulography methods proposed by Baldewsing *et al.* [40] and later by Le Floc'h *et al.* [42] where the detection of inclusions was solely based on radial strains or their spatial derivatives, the proposed segmentation includes the stress distribution, which is iteratively updated by the PFEM. The internal segmentation thus evolves toward the final morphology in a few iterations (see Figs. 3 and 4). Our method allows describing complex morphologies with soft (high strain) and hard (low strain) inclusions without prior knowledge on their number, shape or localization. Because of the interdependency in modulus assessment, an overestimation of the soft component modulus resulted in an underestimation of the modulus of harder constituents.

B. Performance of the Algorithm on Measured Strain Fields

Using measured strain fields from ultrasound simulations and reference contours as preconditioning regions, it was found that the inverse problem overestimates Young's moduli of soft inclusions and underestimates those of calcium inclusions (see Section III-C1). This can be attributed to the inherent smoothing of the strain estimator. As it evaluates the local strain using MWs (MWs = 1 mm × 1 mm), the LSME tends to homogenize strains, decreasing the natural strain variations and thus introduces a bias. This naturally affects the segmentation/optimization procedure in terms of detectability (see Section III-C2) and quantification of Young's moduli (see Section III-C3). Adding noise on RF data, as expected, did not improve the results. Noise creates artefactual strain behavior, which is interpreted as mechanical heterogeneities by the algorithm.

The detectability and quantification of hard inclusions were particularly problematic because the low strain level approached the noise level (see Fig. 5). However, as long as the loading pressure remains sufficient to create sufficient contrast in the measured strain field their detectability and quantification can be ensured (see Fig. 6). Overall, the algorithm was found robust, both in terms of detection and quantification. *In vitro* experiments confirmed the feasibility of such approach. As in the simulations, the detectability of hard inclusions was found more difficult. However, regarding soft inclusions, the detectability and quantification were found promising. Considering the importance of characterizing the lipid pool for vulnerable plaque detection, this reinforces the interest of the proposed method.

C. Can the Proposed Method Detect Vulnerable Plaques?

Rupture prone atherosclerotic plaques or vulnerable plaques possess specific morphological and biomechanical markers such as a large necrotic core covered by a thin fibrous cap, macrophage infiltration, and calcium inclusions [56]. Specific features like fibrous cap thickness and peak cap stress were shown to be markers of vulnerability [12]. A cap thickness below 50 μm, under physiological loading conditions (blood pressure), leads to peak cap stress above 300 kPa, which is the collagen rupturing threshold [6]. Using the proposed NIV-iMod method, we were able to measure cap thickness in the order of 1 mm with an average error of 77 ± 60 μm from real strain fields (see FEM study in Table II), and 172 ± 98 μm for realistic ultrasound simulations (see Field II study in Table II), which is larger than the targeted thickness threshold. However, considering the resolution of the imaging system (the ultrasound wavelength ≈ 200 μm), those results are acceptable. Using higher frequency external probes, one may probably increase the sensitivity of the cap thickness measurement. A precise measurement of the vulnerable cap thickness ($C_{th} \approx 50$ μm) would, however, require high resolution invasive imaging techniques, as high-frequency 60 or 80 MHz IVUS or optical coherence tomography.

Peak cap stress is also highly dependent on the internal morphology of the necrotic core, calcium inclusions and their mechanical properties [12]. A softer necrotic core offers less mechanical resistance and thus increases cap stress. The proposed NIV-iMod method provided a good estimation of the necrotic core morphology and Young's modulus even when considering noise in the acquisition process. Calcium inclusions, however, seemed to be more difficult to detect, especially under low pressure loading conditions. This is mainly due to the fact that materials with larger Young's moduli produce smaller strain fields, which can be challenging for strain estimator [57]. One of the solutions we adopted here was to use a larger pressure step ΔP to compute strain elastograms and use as much information from successive frames (using time-ensemble ultrafast elastograms, as proposed in [30]). One could also adopt the approach of Le Floc'h *et al.* to increase the robustness of the method using elastography-based criteria such as correlation coefficient, displacement, and strain quality [44]. Further developments in that direction would benefit the proposed method.

D. Study Limitations and Potential Improvements

Although original and promising concepts for the characterization of carotid atherosclerotic lesions were presented, several limitations deserve to be pointed out at this stage.

1) The plane strain incompressibility assumption was used in the deformation matrix computation to mitigate the impact of the low lateral resolution of linear

arrays [30]. Even if such assumption is reasonable when the plaque length (along the vessel axis) is large with regards to its radial dimension [11], [12], [58], it would probably not hold for complex 3-D plaque morphologies. Angular strain compounding, as proposed by Hansen *et al.* [59], may be used instead to improve the estimation of lateral deformations without any assumption on mechanical properties. However, as stated in our previous study [30], grating lobe artifacts appear at large beam steered angles and corrupt lateral components of the deformation matrix.

2) Because cross-sectional 2-D ultrasound images were acquired, the plane strain assumption had to be considered to solve the inverse problem, as mentioned above. It is well known that in real conditions, carotid arteries have a complex 3-D geometry and can move and deform outside the imaging plane. In that case, our method would benefit of a 3-D acquisition system [60] coupled with a 3-D segmentation/optimization procedure. In the meantime, 2-D elastography and modulography are incomplete measurement and must be interpreted with caution.

3) In this paper, we only considered the internal loading pressure as a boundary condition inside the vessel wall. The outer contour of the plaque was considered stress free and no surrounding tissue was included in the inverse problem. It is known that the carotid artery may be influenced by external forces, such as the pressure of the probe applied on the patient neck, and by inhomogeneous external boundary conditions as the carotid artery is adjacent to the cervical spine and attached to paraspinal muscles (rigid) on one side, and surrounded by the sternocleidomastoid muscle and compliant jugular vein on the other sides. Le Floc'h *et al.* briefly addressed the impact of surrounding tissues on the efficiency of the inverse problem in the context of IVUS modulography [61]. More recently, our team proposed to extend this approach using measured displacements on the outer contour of the artery as a boundary condition [50]. Further developments in that direction need to be explored to make those models robust to boundary conditions.

4) Even if the proposed method was found relatively efficient, the underlying model remains simple and might be too restrictive for *in vivo* applications. The tissues were assumed to behave linearly as isotropic and incompressible materials. However, it has been shown that vascular tissues have a more complex behavior including anisotropy [34]. Our method could be extended to more complex rheology models. However, to preserve the stability of the inverse problem, one would probably have to introduce more information and priors to constrain the problem. However, as stated in earlier studies [40], [42], [50], considering linear elastic, isotropic and incompressible materials remains acceptable as long as the displacements and strains remain small. More complex tissue models (i.e., nonlinear and anisotropic) might be useful to better describe the mechanical behavior of vascular tissues.

In that case, the stress/strain relationship described in (2) would need to be changed. However, whatever the relationship, the same method (i.e., k-means clustering preconditioner+optimization) would be applied to detect mechanical heterogeneities and identify their mechanical properties. In the case of a multi parametric model (e.g., linear and compressible), the segmentation part might be eased by the fact that the k-means clustering would be performed in N-dimensional space (N being the number of parameters describing the model) and thus could be more discriminative. In the case of a nonlinear model, multiple elastograms (i.e., from multiple loading conditions) would need to be considered. Note that using multiple pressure increments might improve the discriminative power of the k-means algorithm since the number of measurements would be increased.

5) Segmentation of plaque inclusions solely based on measured strains might be insufficient *in vivo* because strain measurements may be altered by the presence of ultrasound shadowing, clutter and electronic noise. To overcome such problems, a multimodality segmentation tool might be envisaged to identify plaque inclusions. Such tool may include the stress/strain ratio (i.e., our AYM criterion) as well as echo amplitude [62] and speckle statistics [63].

6) *In vivo* testing still needs to be performed to assess the feasibility of the approach for clinical applications. *In vivo* vascular modulography is indeed significantly more challenging than the *in silico* and *in vitro* experiments presented in this paper. Although, we demonstrated that noninvasive vascular modulography is feasible *in vitro* (see Fig. 8), more validation has to be performed. Several limitations have to be addressed *in vitro* before attempting *in vivo* experiments. First, the robustness of the elastography and modulography algorithms against out-of-plane motion and deformations has to be validated. The elastography and modulography algorithms presented here are only valid under plane strain conditions. Note, however, that without the plane strain and incompressibility assumptions, the proposed modulography algorithm remains valid but its reliability in the context of noninvasive carotid artery imaging still needs to be proven *in vivo*. Another issue that would need to be considered to assess the real potential of the modulography algorithm *in vivo* is the impact of artefactual image features produced by strong attenuation, shadowing and beam diffraction. Strain artifacts due to clutter noise arising from hyperechoic neighboring regions would also need to be considered. Such artifacts must be discarded before further processing, as proposed by our group in the context of IVUS modulography imaging [44].

V. Conclusion

In this paper, a robust mechanical inverse problem based on NIVE was proposed for the reconstruction of carotid plaque internal morphology and Young's moduli. It was successfully

validated with FEM and measured strain fields from ultrasound simulations and *in vitro* measurements. Further developments should include the extension of the model to 3-D and the incorporation of more realistic boundary conditions.

REFERENCES

[1] A. S. Go *et al.*, "Executive summary: Heart disease and stroke statistics—2013 update: A report from the American Heart Association," *Circulation*, vol. 127, no. 1, pp. 143–152, 2013.

[2] J. L. Fleg *et al.*, "Detection of high-risk atherosclerotic plaque: Report of the NHLBI Working Group on current status and future directions," *JACC, Cardiovascular Imag.*, vol. 5, no. 9, pp. 941–955, 2012.

[3] S. Dai, C. Bancej, A. Bienek, P. Walsh, P. Stewart, and A. Weilgosz, "Tracking heart disease and stroke in Canada 2009," *Chronic Diseases Canada*, vol. 29, no. 4, pp. 192–193, 2009.

[4] W. Casscells, M. Naghavi, and J. T. Willerson, "Vulnerable atherosclerotic plaque: A multifocal disease," *Circulation*, vol. 107, no. 16, pp. 2072–2075, 2003.

[5] P. Libby, P. M. Ridker, and G. K. Hansson, "Progress and challenges in translating the biology of atherosclerosis," *Nature*, vol. 473, no. 7347, pp. 317–325, 2011.

[6] G. Finet *et al.*, "Morphological and biomechanical aspects of vulnerable coronary plaque," *Arch. Maladies Coeur Vaisseaux*, vol. 100, nos. 6–7, pp. 547–553, 2007.

[7] R. Virmani, F. D. Kolodgie, A. P. Burke, A. Farb, and S. M. Schwartz, "Lessons from sudden coronary death: A comprehensive morphological classification scheme for atherosclerotic lesions," *Arteriosclerosis, Thrombosis, Vascular Biol.*, vol. 20, no. 5, pp. 1262–1275, 2000.

[8] J. Ohayon *et al.*, "Necrotic core thickness and positive arterial remodeling index: Emergent biomechanical factors for evaluating the risk of plaque rupture," *Amer. J. Physiol.-Heart Circulatory Physiol.*, vol. 295, no. 2, pp. H717–H727, 2008.

[9] G. C. Cheng, H. M. Loree, R. D. Kamm, M. C. Fishbein, and R. T. Lee, "Distribution of circumferential stress in ruptured and stable atherosclerotic lesions. A structural analysis with histopathological correlation," *Circulation*, vol. 87, no. 4, pp. 1179–1187, 1993.

[10] R. T. Lee, H. M. Loree, G. C. Cheng, E. H. Lieberman, N. Jaramillo, and F. J. Schoen, "Computational structural analysis based on intravascular ultrasound imaging before *in vitro* angioplasty: Prediction of plaque fracture locations," *J. Amer. College Cardiol.*, vol. 21, no. 3, pp. 777–782, 1993.

[11] H. M. Loree, R. D. Kamm, R. G. Stringfellow, and R. T. Lee, "Effects of fibrous cap thickness on peak circumferential stress in model atherosclerotic vessels," *Circulat. Res.*, vol. 71, no. 4, pp. 850–858, 1992.

[12] G. Finet, J. Ohayon, and G. Rioufol, "Biomechanical interaction between cap thickness, lipid core composition and blood pressure in vulnerable coronary plaque: Impact on stability or instability," *Coronary Artery Disease*, vol. 15, no. 1, pp. 13–20, 2004.

[13] J. Ohayon *et al.*, "Influence of residual stress/strain on the biomechanical stability of vulnerable coronary plaques: Potential impact for evaluating the risk of plaque rupture," *Amer. J. Physiol.-Heart Circulatory Physiol.*, vol. 293, no. 3, pp. H1987–H1996, 2007.

[14] J. Ohayon, G. Finet, F. Treyve, G. Rioufol, and O. Dubreuil, "A three dimensional finite element analysis of stress distribution in a coronary atherosclerotic plaque: *In vivo* prediction of plaque rupture location," in *Biomechanics Applied to Computer Assisted Surgery*, vol. 37, Y. Payan, Ed. Kerala, India: Research Signpost, 2005, pp. 225–241.

[15] A. V. Engelen *et al.*, "Multi-center MRI carotid plaque component segmentation using feature normalization and transfer learning," *IEEE Trans. Med. Imag.*, vol. 34, no. 6, pp. 1294–1305, Jun. 2015.

[16] A. Gupta *et al.*, "Evaluation of computed tomography angiography plaque thickness measurements in high-grade carotid artery stenosis," *Stroke*, vol. 45, no. 3, pp. 740–745, 2014.

[17] T. J. Kaufmann and D. F. Kallmes, "Utility of MRA and CTA in the evaluation of carotid occlusive disease," *Seminars Vascular Surg.*, vol. 18, no. 2, pp. 75–82, Jun. 2005.

[18] C. Naim *et al.*, "Vulnerable atherosclerotic carotid plaque evaluation by ultrasound, computed tomography angiography, and magnetic resonance imaging: An overview," *Can. Assoc. Radiologists J.*, vol. 65, no. 3, pp. 275–286, 2014.

[19] A. Fenster, C. Blake, I. Gyacskov, A. Landry, and J. D. Spence, "3D ultrasound analysis of carotid plaque volume and surface morphology," *Ultrasonics*, vol. 44, pp. e153–e157, Dec. 2006.

[20] C. D. Ainsworth, C. C. Blake, A. Tamayo, V. Beletsky, A. Fenster, and J. D. Spence, "3D ultrasound measurement of change in carotid plaque volume: A tool for rapid evaluation of new therapies," *Stroke*, vol. 36, no. 9, pp. 1904–1909, 2005.

[21] A. C. Akyildiz *et al.*, "Effects of intima stiffness and plaque morphology on peak cap stress," *BioMed. Eng. Online*, vol. 10, no. 1, p. 25, 2011.

[22] S. Howarth *et al.*, "Correlation of macrophage location and plaque stress distribution using USPIO-enhanced MRI in a patient with symptomatic severe carotid stenosis: A new insight into risk stratification," *Brit. J. Neurosurg.*, vol. 21, no. 4, pp. 396–398, 2007.

[23] Z.-Y. Li *et al.*, "Stress analysis of carotid plaque rupture based on *in vivo* high resolution MRI," *J. Biomech.*, vol. 39, no. 14, pp. 2611–2622, 2006.

[24] J. Ophir, I. Céspedes, H. Ponnekanti, Y. Yazdi, and X. Li, "Elastography: A quantitative method for imaging the elasticity of biological tissues," *Ultrason. Imag.*, vol. 13, no. 2, pp. 111–134, 1991.

[25] C. L. de Korte *et al.*, "Identification of atherosclerotic plaque components with intravascular ultrasound elastography *in vivo*: A Yucatan pig study," *Circulation*, vol. 105, no. 14, pp. 1627–1630, 2002.

[26] R. L. Maurice, J. Fromageau, É. Brusseau, G. Finet, G. Rioufol, and G. Cloutier, "On the potential of the Lagrangian estimator for endovascular ultrasound elastography: *In vivo* human coronary artery study," *Ultrasound Med. Biol.*, vol. 33, no. 8, pp. 1199–1205, 2007.

[27] Y. Majdouline *et al.*, "Endovascular shear strain elastography for the detection and characterization of the severity of atherosclerotic plaques: *In vitro* validation and *in vivo* evaluation," *Ultrasound Med. Biol.*, vol. 40, no. 5, pp. 890–903, 2014.

[28] S. Korukonda, R. Nayak, N. Carson, G. Schifitto, V. Dogra, and M. M. Doyley, "Noninvasive vascular elastography using plane-wave and sparse-array imaging," *IEEE Trans. Ultrason., Ferroelect., Freq. Control*, vol. 60, no. 2, pp. 332–342, Feb. 2013.

[29] H. H. G. Hansen, A. E. C. M. Saris, N. R. Vaka, M. M. Nillesen, and C. L. de Korte, "Ultrafast vascular strain compounding using plane wave transmission," *J. Biomech.*, vol. 47, no. 4, pp. 815–823, 2014.

[30] J. Porée, D. Garcia, B. Chayer, J. Ohayon, and G. Cloutier, "Noninvasive vascular elastography with plane strain incompressibility assumption using ultrafast coherent compound plane wave imaging," *IEEE Trans. Med. Imag.*, vol. 34, no. 12, pp. 2618–2631, Dec. 2015.

[31] C. Schmitt, G. Soulez, R. L. Maurice, M.-F. Giroux, and G. Cloutier, "Noninvasive vascular elastography: Toward a complementary characterization tool of atherosclerosis in carotid arteries," *Ultrasound Med. Biol.*, vol. 33, no. 12, pp. 1841–1858, 2007.

[32] J. Wan, F. He, Y. Zhao, H. Zhang, X. Zhou, and M. Wan, "Non-invasive vascular radial/circumferential strain imaging and wall shear rate estimation using video images of diagnostic ultrasound," *Ultrasound Med. Biol.*, vol. 40, no. 3, pp. 622–636, 2014.

[33] C. Naim *et al.*, "Characterisation of carotid plaques with ultrasound elastography: Feasibility and correlation with high-resolution magnetic resonance imaging," *Eur. Radiol.*, vol. 23, no. 7, pp. 2030–2041, 2013.

[34] G. A. Holzapfel, G. Sommer, and P. Regitnig, "Anisotropic mechanical properties of tissue components in human atherosclerotic plaques," *J. Biomech. Eng.*, vol. 126, no. 5, pp. 657–665, 2004.

[35] H. H. G. Hansen, G. J. de Borst, M. L. Bots, F. L. Moll, G. Pasterkamp, and C. L. de Korte, "Validation of noninvasive *in vivo* compound ultrasound strain imaging using histologic plaque vulnerability features," *Stroke*, vol. 47, no. 11, pp. 2770–2775, 2016.

[36] K. V. Ramnarine, J. W. Garrard, K. Dexter, S. Nduwayo, R. B. Panerai, and T. G. Robinson, "Shear wave elastography assessment of carotid plaque stiffness: *In vitro* reproducibility study," *Ultrasound Med. Biol.*, vol. 40, no. 1, pp. 200–209, 2014.

[37] M. Couade *et al.*, "Quantitative assessment of arterial wall biomechanical properties using shear wave imaging," *Ultrasound Med. Biol.*, vol. 36, no. 10, pp. 1662–1676, 2010.

[38] J. J. Dahl, D. M. Dumont, J. D. Allen, E. M. Miller, and G. E. Trahey, "Acoustic radiation force impulse imaging for noninvasive characterization of carotid artery atherosclerotic plaques: A feasibility study," *Ultrasound Med. Biol.*, vol. 35, no. 5, pp. 707–716, 2009.

[39] R. A. Baldewsing, J. A. Schaar, F. Mastik, C. W. J. Oomens, and A. F. W. van der Steen, "Assessment of vulnerable plaque composition by matching the deformation of a parametric plaque model to measured plaque deformation," *IEEE Trans. Med. Imag.*, vol. 24, no. 4, pp. 514–528, Apr. 2005.

[40] R. A. Baldewsing, M. G. Danilouchkine, F. Mastik, J. A. Schaar, P. W. Serruys, and A. F. W. van der Steen, "An inverse method for imaging the local elasticity of atherosclerotic coronary plaques," *IEEE Trans. Inf. Technol. Biomed.*, vol. 12, no. 3, pp. 277–289, May 2008.

[41] R. L. Maurice, J. Ohayon, Y. Fretigny, M. Bertrand, G. Soulez, and G. Cloutier, "Noninvasive vascular elastography: Theoretical framework," *IEEE Trans. Med. Imag.*, vol. 23, no. 2, pp. 164–180, Feb. 2004.

[42] S. Le Floc'h *et al.*, "Vulnerable atherosclerotic plaque elasticity reconstruction based on a segmentation-driven optimization procedure using strain measurements: Theoretical framework," *IEEE Trans. Med. Imag.*, vol. 28, no. 7, pp. 1126–1137, Jul. 2009.

[43] S. Le Floc'h, G. Cloutier, G. Finet, P. Tracqui, R. I. Pettigrew, and J. Ohayon, "Vascular imaging modulography: An experimental *in vitro* study," *Comput. Methods Biomech. Biomed. Eng.*, vol. 13, no. S1, pp. 89–90, 2010.

[44] S. Le Floc'h *et al.*, "A four-criterion selection procedure for atherosclerotic plaque elasticity reconstruction based on *in vivo* coronary intravascular ultrasound radial strain sequences," *Ultrasound Med. Biol.*, vol. 38, no. 12, pp. 2084–2097, 2012.

[45] H. H. G. Hansen, M. S. Richards, M. M. Doyley, and C. L. de Korte, "Noninvasive vascular displacement estimation for relative elastic modulus reconstruction in transversal imaging planes," *Sensors*, vol. 13, no. 3, pp. 3341–3357, 2013.

[46] A. A. Oberai, N. H. Gokhale, and G. R. Feijóo, "Solution of inverse problems in elasticity imaging using the adjoint method," *Inverse Problems*, vol. 19, no. 2, p. 297, 2003.

[47] M. S. Richards and M. M. Doyley, "Investigating the impact of spatial priors on the performance of model-based IVUS elastography," *Phys. Med. Biol.*, vol. 56, no. 22, p. 7223, 2011.

[48] H. A. Nieuwstadt *et al.*, "Carotid plaque elasticity estimation using ultrasound elastography, MRI, and inverse FEA—A numerical feasibility study," *Med. Eng. Phys.*, vol. 37, no. 8, pp. 801–807, 2015.

[49] M.-H. R. Cardinal *et al.*, "Carotid artery plaque vulnerability assessment using noninvasive ultrasound elastography: Validation with MRI," *Amer. J. Roentgenol.*, vol. 209, no. 1, pp. 142–151, 2017.

[50] A. Tacheau *et al.*, "The imaging modulography technique revisited for high-definition intravascular ultrasound: Theoretical framework," *Ultrasound Med. Biol.*, vol. 42, no. 3, pp. 727–741, 2016.

[51] R. F. Wagner, S. W. Smith, J. M. Sandrik, and H. Lopez, "Statistics of speckle in ultrasound B-scans," *IEEE Trans. Sonics Ultrason.*, vol. SU-30, no. 3, pp. 156–163, May 1983.

[52] J. A. Jensen, "Field: A program for simulating ultrasound systems," in *Proc. 10th Nordicbaltic Conf. Biomed. Imag.*, 1996, pp. 351–353.

[53] G. Montaldo, M. Tanter, J. Bercoff, N. Benech, and M. Fink, "Coherent plane-wave compounding for very high frame rate ultrasonography and transient elastography," *IEEE Trans. Ultrason., Ferroelect., Freq. Control*, vol. 56, no. 3, pp. 489–506, Mar. 2009.

[54] J. Fromageau, J. L. Gennisson, C. Schmitt, R. L. Maurice, R. Mongrain, and G. Cloutier, "Estimation of polyvinyl alcohol cryogel mechanical properties with four ultrasound elastography methods and comparison with gold standard testings," *IEEE Trans. Ultrason., Ferroelect., Freq. Control*, vol. 54, no. 3, pp. 498–509, Mar. 2007.

[55] G. A. F. Seber, *Multivariate Observations*. Hoboken, NJ, USA: Wiley, 2009.

[56] M. Naghavi, Ed., *Asymptomatic Atherosclerosis: Pathophysiology, Detection and Treatment*. New York, NY, USA: Springer, 2010.

[57] T. Varghese, J. Ophir, E. Konofagou, F. Kallel, and R. Righetti, "Tradeoffs in elastographic imaging," *Ultrason. Imag.*, vol. 23, no. 4, pp. 216–248, 2001.

[58] S. Le Floc'h, G. Cloutier, G. Finet, P. Tracqui, R. I. Pettigrew, and J. Ohayon, "On the potential of a new IVUS elasticity modulus imaging approach for detecting vulnerable atherosclerotic coronary plaques: *In vitro* vessel phantom study," *Phys. Med. Biol.*, vol. 55, no. 19, pp. 5701–5721, 2010.

[59] H. H. G. Hansen, R. G. P. Lopata, and C. L. de Korte, "Noninvasive carotid strain imaging using angular compounding at large beam steered angles: Validation in vessel phantoms," *IEEE Trans. Med. Imag.*, vol. 28, no. 6, pp. 872–880, Jun. 2009.

[60] J. Provost *et al.*, "3D ultrafast ultrasound imaging *in vivo*," *Phys. Med. Biol.*, vol. 59, no. 19, pp. L1–L13, 2014.

[61] S. Le Floc'h, "Modulographie vasculaire: Application à l'identification *in-vivo* du module de Young local des plaques d'athérosclérose," Ph.D. dissertation, Dept. Mech., Univ. Joseph-Fourier, Grenoble, France, 2009.

[62] J. A. Noble, "Ultrasound image segmentation and tissue characterization," *Proc. Inst. Mech. Eng., H, J. Eng. Med.*, vol. 224, no. 2, pp. 307–316, 2010.

[63] F. Destrempes and G. Cloutier, "A critical review and uniformized representation of statistical distributions modeling the ultrasound echo envelope," *Ultrasound Med. Biol.*, vol. 36, no. 7, pp. 1037–1051, 2010.

Jonathan Porée was born in Rennes, France, in 1986. He received the B.Sc. degree in electrical engineering from the National Institute for Applied Sciences (INSA), Rennes, in 2009, the M.Sc. degree in imaging sciences from INSA, Lyon, France, in 2010, and the Ph.D. degree in biomedical engineering from the University of Montreal, Montreal, QC, Canada, in 2016.

He was with the Laboratory of Biorheology and Medical Ultrasonics, University of Montreal Hospital Research Center, University of Montreal. He is currently a Post-Doctoral Fellow with the Langevin Institute, Paris, France. His current research interests include developments in signal and image processing, motion analysis, and biomechanics applied to ultrasound imaging.

Boris Chayer received the bachelor's degree in electrical engineering and the master's degree in biomedical engineering from the École de Technologie Supérieure, Montréal, QC, Canada, in 2001 and 2007, respectively.

He was a Research Engineer for four years at the Institut de Recherches Cliniques de Montreal, Montreal. In 2004, he joined the Laboratory of Biorheology and Medical Ultrasonics, University of Montreal Hospital Research Center, University of Montreal, Montreal. His current research interests are on quantitative ultrasound imaging, elastography, and biomedical phantom designs.

Gilles Soulez is currently a vascular and interventional radiologist with the University of Montreal Hospital, Montréal, QC, Canada. He is also a Professor of radiology and the Chair of the Department of Radiology, Radio-oncology, and Nuclear medicine with the University of Montreal, Montreal, where his research program conducted at the University of Montreal Hospital Research Center is exclusively dedicated to vascular and interventional radiology with a particular interest in the field of vascular ultrasound elastography to characterize vascular vulnerability, aneurysm endovascular repair, peripheral vascular disease, and advanced image guidance for interventional radiology procedures.

Jacques Ohayon received the Ph.D. degree in cardiac mechanics from University Paris 12 (UPVM), France, in 1985.

From 1985 to 1988, he was a Visiting Fellow at the NIH, Bethesda, MD, USA. In 1988, he joined the UPVM as an Assistant Professor of mechanics. He was appointed as a full Professor of mechanics with the Mechanical Engineering School Polytech Annecy-Chambéry, University of Savoie Mont-Blanc, Chambéry, France, in 1993. Since 2003, he has been with the Laboratory TIMC-CNRS UMR 5525, Grenoble, France, where he performs research with his group, the team Cellular/Tissular Dynamics and Functional Microscopy. From 2006 to 2007, he was an Invited Senior Scientist at the Laboratory of Integrative Cardiovascular Imaging Science, NIH, Bethesda. The aims of his research on cardiovascular biomechanics are to understand the evolution of atherosclerotic plaque vulnerability and initiation, and to increase knowledge of the plaque growth process through the combined use of mechanical modeling based on the nonlinear continuum mechanics theory, finite-element method, together with clinical and biological investigations. He has authored more than 120 peer-reviewed articles in these fields and has four patents. Currently, he coordinates an interdisciplinary international scientific consortium on the Biomechanics of Atherosclerosis (initiated during his sabbatical at the NIH in 2007) and with which he already authored more than 40 collaborative studies. He has authored (with one of his colleague Dr. Y. Payan, Ph.D.) a book entitled "*Biomechanics of Living Organs: Hyperelastic Constitutive Laws for Finite Element Modeling*" that was published in 2017.

Guy Cloutier (S'89–M'90–SM'07) received the B.Eng. degree in electrical engineering from the Université du Québec à Trois-Rivières, Trois-Rivières, QC, Canada, in 1984, and the M.Sc. and Ph.D. degrees in biomedical engineering from the École Polytechnique of Montreal, Montréal, QC, Canada, in 1986 and 1990, respectively.

From 1990 to 1992, he was a Post-Doctoral Fellow at The Pennsylvania State University, State College, PA, USA, with Prof. K. Kirk Shung. He is currently the Director of the Laboratory of Biorheology and Medical Ultrasonics, University of Montreal Hospital Research Center, University of Montreal; a Professor with the Department of Radiology, Radio-oncology, and Nuclear Medicine, University of Montreal; and a member of the Institute of Biomedical Engineering, University of Montreal. He has authored more than 185 peer-reviewed articles in his research fields, has eleven active patents, and licensed three technologies. His research interests are in quantitative ultrasound imaging, quasi-static and dynamic ultrasound elastography, development of multi-physics imaging methods, and biomechanical modeling.

Dr. Cloutier was a recipient of the National Scientist Award of the Fonds de la Recherche en Santé du Québec during 2004–2009. He is an Associate Editor of the IEEE TRANSACTIONS ON ULTRASONICS, FERROELECTRIC, AND FREQUENCY CONTROL, an Invited Associate Editor of *Medical Physics* and *PlosOne*, an Editorial Board Member of *Current Medical Imaging Reviews*, and was a Member of the International Advisory Editorial Board of *Ultrasound in Medicine and Biology* for 15 years.